Spatially-resolved investigation of CO_2 methanation over Ni/γ-Al_2O_3 and $Ni_{3.2}Fe$/γ-Al_2O_3 catalysts in a packed-bed reactor

Akash Bhimrao Shirsath[a,1], Mariam L. Schulte[a,b,1], Bjarne Kreitz[c], Steffen Tischer[b], Jan-Dierk Grunwaldt[a,b], Olaf Deutschmann[a,b] *

[a] *Institute for Chemical Technology and Polymer Chemistry (ITCP), Karlsruhe Institute of Technology (KIT), 76131 Karlsruhe, Germany*

[b] *Institute of Catalysis Research and Technology (IKFT), Karlsruhe Institute of Technology (KIT), 76344 Karlsruhe, Germany*

[c] *School of Engineering, Brown University, Providence, Rhode Island 02912, United States*

[1] *Shared first authorship*

** Corresponding Author:*

Olaf DEUTSCHMANN

Bldg. 11.21, KIT-Campus South, Engesserstr. 20, 76131, Karlsruhe, Germany

Tel.: +49 721 608-43064

Fax: +49 721 608-44805

E-mail: deutschmann@kit.edu

Abstract:

CO_2 methanation via the Sabatier reaction with (green) H_2 is promising due to its role in achieving a carbon-neutral energy balance in the context of Power-to-Gas technologies. Since Ni-based catalysts are relatively inexpensive compared to other metals and exhibit high catalytic activity, they are most commonly used. Due to the exothermic nature of the reaction, strong temperature and concentration gradients occur, which influence the catalyst structure. Thus, revealing the effects of structural changes of the catalyst along the reactor bed on local activity and selectivity is essential. A 1D packed-bed reactor model used for numerical simulations, coupled with detailed microkinetics and mass transport limitations. The simulation results are compared with axially-resolved concentration and temperature profiles over 17 wt% Ni/γ-Al_2O_3 and 17 wt% $Ni_{3.2}Fe$/γ-Al_2O_3 catalysts at oven temperatures of 623 K and 723 K. Using additional information from structural spatially-resolved synchrotron-based *operando* X-ray adsorption spectroscopy studies, the oxidation state of Ni was considered in modeling the reactor by changing the catalytically active surface area along the reactor. Predicted surface coverages are compared with surface species experimentally determined by diffuse reflectance infrared Fourier transform spectroscopy. Overall, this study demonstrates the importance of combining modeling with spatially-resolved and temperature-dependent experiments to improve multiscale models and make predictions more accurate.

Keywords:

CO_2 methanation; Catalytic oxidation; Ni-Fe/Al_2O_3; Chemical Kinetics; Operando characterization; Spatially-resolution of fixed bed reactor.

1. Introduction

Carbon dioxide (CO_2) emissions from fossil fuel combustion increase concerns about global climate change, resulting in increased interest worldwide in reducing GHG emissions, particularly CO_2 [1]. However, CO_2 is a convenient, inexpensive, and abundant source of C_1 for chemical processes [2–4]. To meet the world's increasing energy demands, its transformation into fuel with renewable hydrogen from electrolysis provides solutions to the problem of global warming [5,6]. In many parts of the world, a natural gas pipeline already exists for the storage of renewable energy, and the production of synthetic natural gas (SNG) from hydrogen derived from electrolyzers is of particular interest for the storage of renewable electrical energy in the form of hydrocarbons [7–9]. In the last decade, research efforts have been focused on developing catalysts which are able to utilize this excess renewable hydrogen to reduce dependence on fossil fuels. CO_2 released from industrial flue gases can be hydrogenated with these catalysts [10], a closed carbon cycle can be created [11,12]. Methanation of CO_2 via the Sabatier reaction (Eq. (1)) with (green) H_2 is promising in terms of achieving a carbon-neutral energy balance in the context of Power-to-Gas process [4,9,13–15].

$$\mathrm{CO_2 + 4H_2 \rightleftharpoons CH_4 + 2H_2O}, \qquad \Delta_R H_{298\,K} = -165.0\ \mathrm{kJ\ mol^{-1}} \tag{1}$$

Due to the exothermic nature of the Sabatier reaction, lower temperatures favor the formation of CH_4 [4]. However, the reaction is kinetically hindered and needs highly active catalysts [16]. Nickel-based catalysts are commonly used because they are relatively inexpensive and highly efficient [4,14,15,17–20]. The catalyst activity and stability depend on the choice of metal oxide used as support [21–23], and Al_2O_3-supported catalysts offer the highest CH_4 yield because of the presence of basic adsorption sites[24–27]. One drawback of Ni-based catalysts is the deactivation by oxidation [4]. Mutz et al. [28,29] and Vogt et al. [30,31] observed that Ni/γ-Al_2O_3 catalysts, in the presence of O_2 impurities in the feed, experienced strong deactivation during fluctuating CO_2 methanation conditions which resembles the transient availability of renewable energies. Partial oxidization of the Ni catalyst can be prevented by removing water or traces of oxygen in the feed and reactivation can be achieved by re-reduction [32]. Recently, it has been demonstrated that combining Fe with Ni to improve the catalytic performance of a methanation catalyst under steady-state and dynamic conditions is a promising strategy to improve its stability and performance [20,33,34]. This observation has been predicted for CO hydrogenation by theoretical modeling first [4,10,21,35,36]. However, during CO_2 methanation, the Ni-Fe alloy structure is dynamic. The Ni phase remains reduced while Fe oxidizes [37–39]. Using ex-situ studies, Burger et al. concluded that Fe segregates to surface of the particles under Fe^{2+}

93 formation, which might provide the particle surface with redox active sites that could enhance CO_2
94 activation under certain conditions [33].

95 At an industrial level, CO_2 methanation is generally performed in fixed-bed reactors [40–42]. It is
96 expected that strong thermal and concentration gradients will form along the catalyst bed due to the
97 highly exothermic nature of the Sabatier reaction. At 473-773 K, the highly exothermic CO_2
98 methanation reaction is thermodynamically favored [43]. However, at temperatures above 623 K, CO
99 is produced as by product due to the endothermic reverse water-gas shift reaction (Eq. (2)) which
100 reduces CH_4 yield.

$$\mathrm{CO_2 + H_2 \rightleftharpoons CO + H_2O}, \qquad \Delta_R H_{298\,K} = 41.0\ \mathrm{kJ\ mol^{-1}} \tag{2}$$

101 As Ni-Fe systems are exceedingly dynamic, gradients can affect the catalyst structure, resulting in
102 deactivation phenomena, e.g. thermal degradation and oxidation [44–46]. Consequently, a detailed
103 understanding of the reactions taking place along the catalyst bed will be essential for determining
104 changes in the catalyst composition, activity and selectivity [36,46–48]. The high exothermicity of the
105 process necessitates the consideration of heat management and the coupling of heat and mass
106 transfer to describe the Sabatier process [49–51]. Additionally, the high reaction rate under
107 methanation conditions might affect catalyst performance due to transport limitations. Although CO_2
108 methanation occurs in a simple way, it is difficult to establish the mechanism of the reaction since
109 various intermediates have been reported and the rate-determining step may change at different
110 conditions [4,14,19,41,52]. For CO_2 methanation, three pathways have been identified: the
111 carbide/redox pathway with CO* formation via direct CO_2 dissociation, and the H-assisted CO_2*
112 dissociation pathway via carboxyl or formate [33,37,40,53–59]. Different reactor concepts were
113 developed due to the thermodynamic limitations of methanation reaction and catalyst deactivation
114 at high temperatures, which makes handling the large heat release rate a challenge even at steady
115 state [52,58,60,61]. Most often fixed-bed reactors are used in power-to-gas plants. A number of fixed-
116 bed reactor models have been reported in the literature, most of which rely on a 1D [62,63] or 2D
117 [49,50] homogeneous or heterogeneous models as 3D [41,64–66] ones require longer computational
118 time. Furthermore, only a few models incorporate detailed chemical kinetics and catalyst structural
119 information [67].

120 In this work, we examine the Sabatier reaction on a 17 wt% Ni/γ-Al_2O_3 and a 17 wt% $Ni_{3.2}Fe$/γ-Al_2O_3
121 catalyst by comparing modeling results with experimental data. The aim of this study is to analyze the
122 concentration profiles and surface coverages in a packed-bed reactor using a 1D heterogeneous

reactor model with detailed surface chemical kinetics scheme for the methanation of CO and CO_2 over Ni-based catalyst proposed by Schmider et al. [42]. The 1D approach is used as a viable compromise between computational costs and physical accuracy, and the model is used to compute spatially-resolved reaction rates and surface coverages. Axially-resolved experiments served as a basis to evaluate the model and additional structural information along the catalyst bed from operando X-ray absorption spectroscopy (XAS) was employed to improve the simulation results. For further model validation, predicted surface coverages were substantiated with diffuse reflectance infrared Fourier transform spectroscopy (DRIFTS) studies.

2. Experiments

2.1. Catalyst preparation and characterization

A 17 wt% Ni/γ-Al_2O_3 and 17 wt% $Ni_{3.2}Fe$/γ-Al_2O_3 catalyst were prepared through homogeneous precipitation with urea over an 18 h period. Thereafter, the solids were washed and dried overnight at 383 K, followed by 4 h of calcination under static air conditions at 773 K (5 K min^{-1}). N_2-physisorption yielded a specific surface area of ≈220 m^2 g^{-1} for both catalysts. The 17 wt% metal loading was confirmed by inductively coupled plasma optical emission spectroscopy (ICP-OES), and a metal particle diameter of 3.8±0.9 nm was determined by transmission electron microscopy (STEM) for both catalysts. A more detailed description of catalyst preparation and characterization can be found elsewhere [20,48].

2.2. Catalyst testing

Kinetic experiments were conducted on a recently developed lab-scale test setup that enables simultaneous acquisition of spatially-resolved temperature and concentration profiles. A schematic representation of the experimental setup used for these axially-resolved measurements along the catalyst bed for the CO_2 methanation is shown in Figure 1. Serrer et al. [48] provide an in-depth description of the experimental setup and the performed measurements. Here we will only briefly describe the setup.

The powdered catalyst was first pressed and then sieved into a fraction of 300-450 µm. A 36 mm catalyst bed was obtained by filling a glass quartz reactor (inner diameter 6 mm, length 33 cm) with 250 mg of catalyst diluted with SiC in a ratio of 1:4. A glass capillary with two sampling holes (Polymicro technologies, 60 cm length and 320 µm inner diameter) was placed in the center of the reactor to record the temperature through a type K thermocouple in the capillary and enable sampling of axial concentrations. Both, oven and reactor were mounted on a motorized linear stage setup (Zaber), whereas the capillary was fixed at both ends. The oven reactor unit was then moved during the

experiments to obtain axially resolved measurements. A micro GC (Agilent 490) was used for qualitative analysis of the total gas composition via end-of-pipe measurements and mass flow controllers (Bronkhorst) to tune the gas flow. A mass spectrometer (MS) (ThermoStar GSD 320, Pfeiffer Vacuum) was used to analyze the gas composition in the capillary at the sampling orifice. A gas-phase mixture at the rate of 500 mL min^{-1} containing 25 vol% of CO_2 and H_2 in a ratio of 4:1 in N_2 was fed into the reactor under atmospheric conditions. Prior to the experiments, the catalyst was reduced with 50% H_2 in N_2 at 773 K for 2 h.

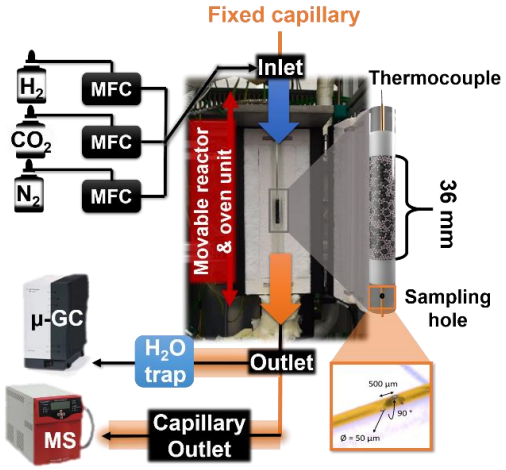

Figure 1: Experimental setup for spatially-resolved activity measurements along the catalyst bed.

2.3. Spatially-resolved *operando* XAS

A spatially-resolved structural analysis of the catalysts was achieved through *operando* X-ray absorption spectroscopy (XAS). The experiments were conducted in quartz microreactors [68] containing a packed bed with 1 cm length filled with sieved 100-200 µm catalyst particles of either the 17 wt% Ni/γ-Al_2O_3 or 17 wt% $Ni_{3.2}Fe$/γ-Al_2O_3, diluted with γ-Al_2O_3 in a ratio of 1:1.3, as shown in Figure 2.

Gases were analyzed using a micro-GC (Agilent 490) and a MS (ThermoStar GSD 320, Pfeiffer Vacuum) after being heated using a hot air blower (Oxford GSB-1300) [69]. The catalysts were activated at 773 K for 2 h with H_2:N_2 in a 1:1 ratio prior to the XAS experiment at ambient pressure. For the catalytic activity measurements, the catalysts were heated under reducing conditions to the desired temperature and then switched to CO_2 methanation conditions (50 mL min^{-1}, 25% H_2:CO_2 = 4:1, N_2) to test their catalytic activity. XAS measurements were performed at the SuperXAS beamline at the Swiss Light Source, Paul Scherrer Institute (PSI) in a quick scanning XAS (QEXAFS) mode [70]. The catalyst bed in quartz capillary was measured at three different positions, beginning, centre, and end. Quick

EXAFS spectra were acquired at Ni and Fe K-edges (for more details on the XAS measurements, cf. ref. [48]).

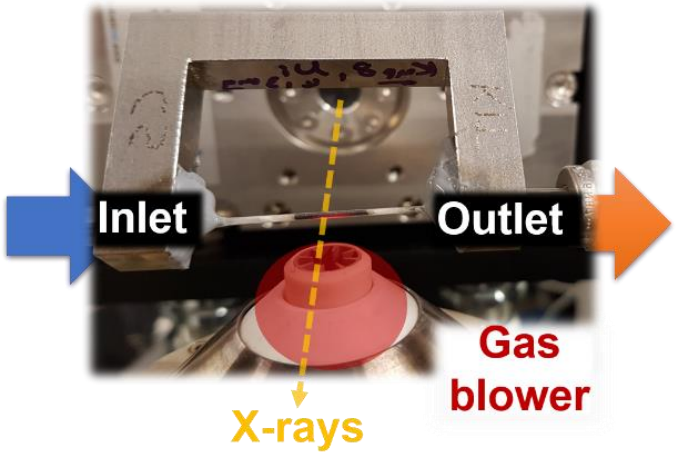

Figure 2: Micro capillary reactor setup for quick EXAFS experiments.

2.4. DRIFT spectroscopy

A commercial Bruker Vertex 70 FT-IR spectrometer equipped with a Hg-Cd-Ted detector and cooled by liquid nitrogen was utilized for the diffuse reflectance Fourier transform infrared spectroscopy (DRIFTS) measurements. Prior to the DRIFTS measurements, the catalyst was pre-reduced in 50% H_2/N_2 for 2 h at 773 K. A Harrick Praying™ high-temperature reaction cell was used to clean the surface of pre-reduced catalysts at 673-723 K over 2 h at a N_2:H_2 ratio of 1:1. DRIFTS spectra were measured under CO_2 methanation conditions (115 mL min^{-1}, 25 vol% H_2:CO_2=4:1 in N_2) at 523, 623, and 723 K. More information on the DRIFTS setup is provided in ref. [48].

3. Modeling approach and numerical simulation

3.1. Simulation of spatially-resolved concentration profiles

CO_2 methanation experiments were modeled and simulated within the DETCHEM software package [71–73]. The CO_2 methanation experiments are simulated with a 1D heterogeneous packed-bed reactor model using a continuum modeling approach. Under the assumption that no changes occur in the radial fluid properties, one-dimensional equations for the mass, species, and heat balance can be solved. In addition, our model includes fluid-solid heat and mass transfer. Equation (3) shows the continuity equation. Due to total mass conservation under steady-state conditions, the right-hand side term of Eq. (3) is equal to zero.

$$\frac{d\rho u}{dz} = a_{\mathrm{v}} \sum_{i \in S_{\mathrm{g}}} M_i R_i^{\mathrm{surf}} \tag{3}$$

where u is the superficial velocity of gas, R_i^{surf} is the effective molar production of rate of gas-phase species i by surface reaction, a_{v} is the ratio of particle surface area to reactor volume, M_i is the molar mass of species i, ρ is the gas-phase density, z is the axial coordinate, and S_{g} is the set of gas-phase species. The species mass balance is given in Eq. (4).

$$\rho u \frac{dY_i}{dz} = a_{\mathrm{v}} \left(M_i R_i^{\mathrm{surf}} - Y_i \sum_{j \in S_{\mathrm{g}}} M_j R_j^{\mathrm{surf}} \right) \tag{4}$$

where Y_i is the mass faction of gas-phase species i. In present modeling approch, external fluid-solid mass transfer is included through Eq. (5). By considering the external fluid-solid mass transfer coefficient $k_{i,\mathrm{fs}}$, the approximated resistance to species mass transport is calculated more precisely between the composition at the catalyst surface and the mean composition.

$$M_i R_i^{\mathrm{surf}} = k_{\mathrm{fs},i} \left(\rho_{\mathrm{s},i} Y_{\mathrm{s},i} - \rho_i Y_i \right) \tag{5}$$

DETCHEM$^{\mathrm{PBR}}$ includes various empirical correlations for the calculation of the mass transfer at fluid-solid interface. For calculation of $k_{\mathrm{fs},i}$, the method proposed by Gnielinski et al. [74–76] was used, assuming the catalyst bed consists of spherical particles (see SI from Eqs. (S1)-(S9)). The pressure drop in the reactor is calculated via Eq. (6).

$$\frac{dp}{dz} = f \frac{\rho u^2}{d_{\mathrm{p}}} \tag{6}$$

where p is the pressure, f is the friction factor, and d_{p} is the particle diameter. The friction factor f is calculated based on Ergun equation [77], as shown in Eq. (7).

$$f = \frac{(1-\varepsilon)}{\varepsilon^3} \left[150 \frac{(1-\varepsilon)\mu}{\rho u d_{\mathrm{p}}} + 1.75 \right] \tag{7}$$

where μ is the fluid viscosity, and ε is the bed porosity. For the present simulation study, no energy balance is solved. Instead, the actual measured temperature profile in the reactor is used via an additional subroutine. Although an energy balance is not solved in this study, for reference purposes, the energy balance equations for the gas and solid phase are provided in the SI (see Eqs. (S10)-(S11)).

3.2. Chemical kinetics

The flow model is coupled with a thermodynamically consistent microkinetic surface reaction scheme proposed by Schmider et al. [42] to compute spatially-resolved reaction rates and surface coverages. Schmider et al. [42] validated their derived microkinetic model against several published studies and achieved a good agreement across all experiments. The mean-field microkinetic model contains 19 species and 42 reactions for the methanation of CO and CO_2 over Ni-based catalyst. Methanation of CO_2 is described by a direct dissociative pathway that involves CO* and a hydrogen-assisted pathway that involves carboxyl (COOH*) as an intermediate. The effective molar production rate R_i^{surf} of gas-phase species i by surface phase reaction is calculated using Eq. (8).

$$R_i^{\mathrm{surf}} = \eta_i F_{\mathrm{cat/geo}} \dot{s}_i \tag{8}$$

where η_i is the effectivness factor of gas-phase species i, $F_{\mathrm{cat/geo}}$ is the ratio of active catalytic surface area to the geometric surface area of the catalyst particle, and $\dot{s}_i$ is the molar production rate of gas-phase species i by surface reaction (Eq. (9)).

$$\dot{s}_i = \sum_{k \in R_{\mathrm{s}}} \nu_{ik} k_k \prod_{j \in S_{\mathrm{g}} \cup S_{\mathrm{s}}} c_j^{\nu'_{jk}} \tag{9}$$

where R_{s} and S_{s} are the sets of surface reactions and surface species, respectively, ν_{ik} are stoichiometric coefficients, ν'_{jk} are the reaction orders (equal to the stoichiometic coefficient of the reactants), and c_i is the concentration of species i given as mol m^{-2} for adsorbed species and mol m^{-3} for gas-phase species and k_k represent the rate constant of reaction k. The mean-field approximation enables the modeling of local interactions between adsorbate and their effect on k_k by incorporating an extra factor in the Arrhenius expression, represented as Eq. (10).

$$k_k = A_k T^{\beta_k} \exp\left(-\frac{E_{\mathrm{a},k}}{RT}\right) \prod_{i \in S_s} \exp\left(\frac{\epsilon_{ik}\theta_{ik}}{RT}\right), \tag{10}$$

where A_k is the pre-exponential factor, β_k is a temperature dependency parameter, θ_{ik} is the surface coverage of species i in reaction k, $E_{\mathrm{a},k}$ is the activation energy of reaction k, ϵ_{ik} is the coverage dependency of the activation energy, T is temperature and R is the universal gas constant. For adsorbed species, surface concentrations can be written in terms of fractional surface coverages θ_i of species i, via Eq. (11).

$$\theta_i = \frac{\sigma_i c_i}{\Gamma_{\mathrm{cat}}}, \tag{11}$$

where σ_i is the number of sites occupied by the one particle of the species i, Γ_{cat} is the surface site density of active catalyst surface area (mol m^{-2}). The actual amount of catalytically active surface area is considered via $F_{\mathrm{cat/geo}}$, the ratio of active catalytic surface area to the geometric surface area of the catalyst particle, described in Eq. (12). The catalytic surface area A_{cat} is the microscopic area provided by the active catalyst for the catalytic reaction, whereas the geometric surface area A_{geo} is the microscopic area of the gas-phase surface interface of the particles. $F_{\mathrm{cat/geo}}$ is calculated from measured dispersion D via CO chemisorption.

$$F_{\mathrm{cat/geo}} = \frac{A_{\mathrm{cat}}}{A_{\mathrm{geo}}} = \frac{D n_{\mathrm{cat}}}{\Gamma_{\mathrm{cat}} A_{\mathrm{geo}}}, \tag{12}$$

where n_{cat} is the molar amount of active catalyst. For present study, the microkinetic surface reaction scheme by Schmider et al. [42] was used unmodified for simulating both Ni/γ-Al_2O_3 and $Ni_{3.2}Fe$/γ-Al_2O_3 catalyst systems.

3.3. Mass transfer

Since a reaction-diffusion model is computationally expensive, a zero-dimensional diffusion is used instead [78–81]. The model considers the mass transport limitation by pore diffusion within the spherical particles based on the effectiveness factor η approach, calculated as described in Eq. (13) [82,83].

$$\eta_i = \frac{3}{{\phi_i}^2}(\phi_i \coth \phi_i - 1) \tag{13}$$

The Thiele modulus ϕ for species i is calculated using Eq. (14).

$$\phi_i = \frac{d_{\mathrm{pore}}}{2}\sqrt{\frac{k_{\mathrm{eff},i}}{D_{\mathrm{eff,i}}}} \tag{14}$$

where k_{eff} is the effective rate constant for an assumed first-order reaction of species i. The ϕ is utilized to determine the η with the assumption that CO_2 is the limiting species, as its diffusion coefficient is smaller compared to H_2 which diffuses much faster. This assumption is in line with previous literatures approch [49,62,63]. The effective diffusion coefficient $D_{\mathrm{eff},i}$ of species i is

calculated taking into account both effective Knudsen diffusion $D_{\mathrm{knud},i}$ and molecular diffusion $D_{\mathrm{mol},i}$ (see SI Eqs. (S12)-(S14)).

3.4. Numerical solution algorithms

The 1D packed-bed reactor model was implemented as FORTRAN code and coupled with the DETCHEM software package [71,73]. The system of equations was solved numerically along the reactor axis with inlet boundary conditions (provided in Table S1), using the differential-algebraic solver (LIMEX) [84]. Properties such as density, viscosity, specific heat, molar weight, velocity, pressure, surface reaction rates and mass transfer coefficients were updated after each integration step.

4. Results

4.1. XAS analysis

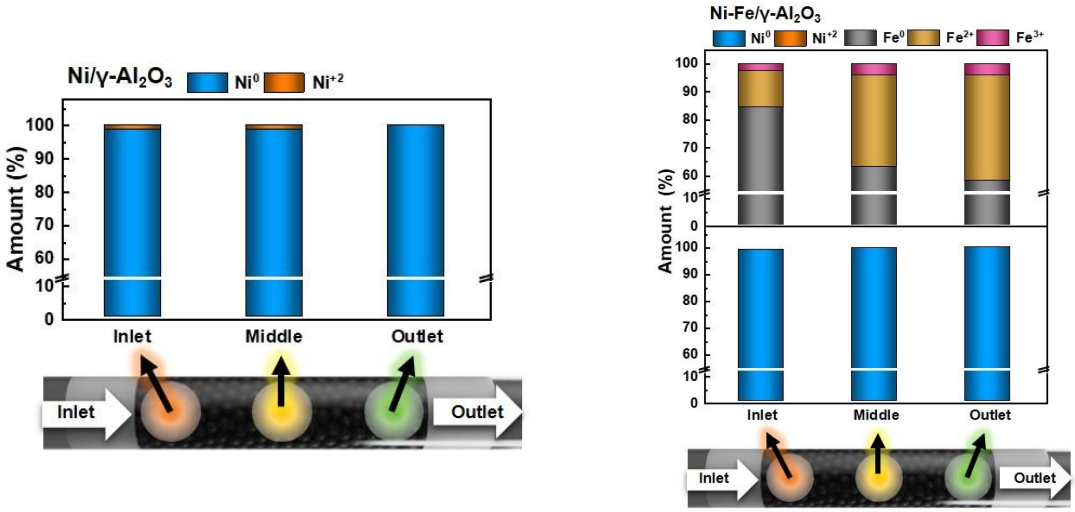

(a) (b)

Figure 3: Relative changes in oxidation state of the (a) 17 wt% Ni/γ-Al_2O_3 and (b) 17 wt% $Ni_{3.2}Fe$/γ-Al_2O_3 catalyst at inlet, middle, and outlet position of the reactor, calculated by linear combination analysis of measured XANES spectra. Adapted and reproduced with permission from ref. [48] under Creative Common Attribution License.

Structural information about the catalyst and present surface species are necessary to validate and improve the 1D packed-bed reactor model. Therefore, the recently published *operando* XAS and DRIFTS results by Serrer et al. [48] are used in this part to be able to follow the further steps. *Operando* QEXAFS measurements were performed to monitor structural changes along a fixed-bed micro reactor at three different positions (inlet, middle, and outlet) during CO_2 methanation at 623 K. The study was

performed for monometallic Ni and bimetallic Ni-Fe catalysts and the results are shown in Figure 3. Ni/γ-Al_2O_3 shows the generation of small amounts of Ni^{2+} at the inlet and middle (≤1.5%), whereas the outlet remains reduced (Figure 3 (a)). The $Ni_{3.2}Fe$/γ-Al_2O_3 showed a similar trend but much smaller changes in the relative degree of oxidation of the Ni (Figure 3 (b)).

In contrast, large degrees of Fe oxidation were observed. A relative increase in Fe^{2+} was measured from 13%, 33%, and 38% between inlet, middle, and outlet, respectively. Consequently, Fe and Ni oxidation along the catalyst bed followed a reverse trend indicating that Fe prevents Ni from oxidation. Thus, the increase in stability of active Ni^0 due to the addition of Fe was confirmed [85]. FeO_x clusters were observed in previous studies, which are highly dynamic and enhance CO_2 activation [36,48]. Along the catalyst bed, an increase in FeO_x species concentration is found. The oxidation of active sites along the catalyst bed during the reaction reduce the active surface area. This dynamic transformation of the active site has to be considered in the microkinetic model for a thorough description of the catalyst morphology [9,86]. It is possible to include this information from *operando* experiments into the model by considering the actual catalytically active surface area as a function of bed length.

4.2. DRIFTS analysis

Surface species information is essential for the evaluation of microkinetic modeling results. DRIFTS is well-suited for this purpose and we extended a study that was performed by Serrer et al. [48] under CO_2 methanation conditions over the Ni/γ-Al_2O_3 and $Ni_{3.2}Fe$/γ-Al_2O_3 catalyst. Additional DRIFT spectra were recorded at 723 K for Ni/γ-Al_2O_3 within this work and the spectra are shown in Figure 4.

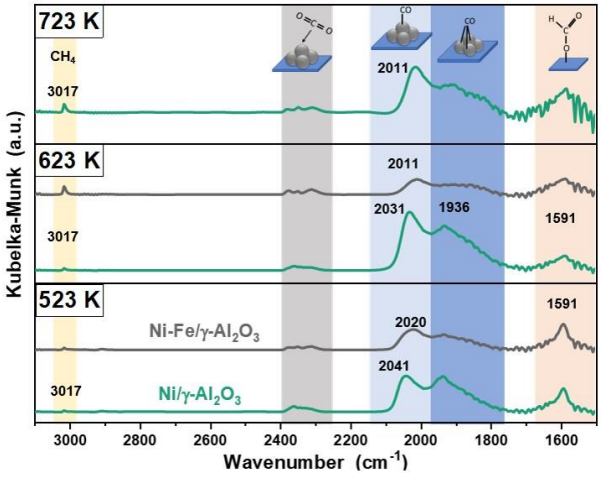

Figure 4: DRIFT spectra of 17 wt% Ni/γ-Al_2O_3 (green line) at 523 K, 623 K and 723 K and 17 wt% $Ni_{3.2}Fe$/γ-Al_2O_3 (gray line) catalyst at 523 K and 623 K during CO_2 methanation.

The C-H stretching vibrations of CH_4* were detected at 3017 cm^{-1}. At 623 K, it has been observed that the CH_4* band intensity is higher for the $Ni_{3.2}Fe/\gamma\text{-}Al_2O_3$ catalyst compared to the $Ni/\gamma\text{-}Al_2O_3$ catalyst indicating a higher activity for the Ni-Fe system. C-H stretching intensity increases with increasing temperature for the $Ni/\gamma\text{-}Al_2O_3$.

At 523 K, the DRIFT spectra of $Ni/\gamma\text{-}Al_2O_3$ show the formation of formate (HCOO*) at 1591 cm^{-1} and CO* intermediates (linear 2041 cm^{-1} and bridged 1936 cm^{-1} CO*), which leads to the conclusion that CO_2 activation takes place via a combination of the H-assisted and direct CO_2 dissociation pathway. According to Galhardo et al. [87], formate can act as a spectator species and does not participate in the reaction. Lim et al. [88] proposed that, HCOO* species are more strongly bound to the surface of catalysts than CO*, which makes them less reactive for further hydrogenation. The intermediate COOH* is postulated to be more reactive compared to HCOO* in the H-assisted pathway [32,42,87–89]. DRIFT analysis performed by Weber et al. [90] at 303 K showed the formation of both intermediates HCOO* and COOH* on a $Ni/\gamma\text{-}Al_2O_3$ catalyst. With increasing temperature, CO_2 hydrogenation is initiated, resulting in a decline in coverages. DRIFTS spectra in this study are recorded at higher temperatures than 303 K and COOH* is not observed, possibly because of its high reactivity and the corresponding short lifetime. In contrast, the HCOO* species tend to accumulate on the catalyst surfaces at lower temperatures (523 K) due to their higher stability (Figure 4). The entropy term of adsorbates increases at higher temperatures, which decreases the binding strenght and leads to desorption. Therefore, the intensity of the formate band decreases. The H-assisted pathway via formation of COOH* is often reported to be in competition with the unassisted dissociation of CO_2* [32,89]. With increasing temperature, terminally adsorbed CO* increases, while bridged CO* species remain unchanged. Thus, at increased temperatures, direct dissociation of CO_2* to CO* is strongly favored in agreement with microkinetic modeling studies [30,32,89].

A shift in the DRIFTS band from 2041 cm^{-1} at 523 K over 2031 cm^{-1} at 623 K to 2011 cm^{-1} at 723 K indicates oxidation of surface Ni^0 to Ni^{2+} [56,91,92]. As shown by the QEXAFS measurement (see Figure 3), the oxidation of Ni surface sites occurs primarily at the start and middle of the catalyst bed. This can be a result of CO_2* dissociation forming O* and CO*, where the adsorbed O* leads to oxidation [36]. Another possible explanation is the presence of O_2 and H_2O impurities in the feed [23]. DRIFT spectra of the $Ni_{3.2}Fe/\gamma\text{-}Al_2O_3$ (Figure 4) catalyst show a similar intensity for the formate band as for the monometallic catalyst. This suggests that Fe does not promote H-assisted CO_2 dissociation pathways. Despite the reduced amount of Ni atoms on the catalyst, there was no change in the intensity of the formate band. This could point to the formation of formate on the hydroxylated alumina surface or the FeO_x surface, which can explain the large reservoir [50,89]. A decrease in CO*

band intensity was observed at 623 K compared to the monometallic catalysts. Therefore, the presence of Fe on the catalyst surface inhibits CO* formation or CO adsorption due to a reduction of exposed Ni surface area. The addition of Fe leads to a lower degree of oxidation of surface Ni atoms, consistent with results from previous studies [55,85]. One hypothesis is that O* diffuses to the Fe clusters, where it leads to FeO_x formation. This agrees with previous studies showing a highly dynamic FeO_x morphology in the bimetallic catalysts [36,48]. Moreover, CO_2 adsorbs preferably on FeO_x clusters since it offers an adsorption site with high basicity [24,25]. The dynamic redox nature of FeO_x clusters (wustite Fe(II) like structure and Fe(III)) promotes the dissociative CO_2* activation and protects Ni from adsorbed CO_2* or CO* [36,48,85]. Due to the protective effect of Fe, CO_2 methanation activity is higher for a bimetallic catalyst.

As discussed above and shown by DRIFTS results, CO_2 methanation over both (Ni/γ-Al_2O_3 and $Ni_{3.2}Fe$/γ-Al_2O_3) catalysts occurs primarily through a combination of the H-assisted and direct CO_2* dissociation pathways. Consequently, the microkinetic model proposed by Schmider et al. [42] for Ni-based catalysts is applied in the present simulation study.

4.3. Experimental results

The microkinetic model and computer code were used to numerically simulate spatially-resolved CO_2 methanation experiments. We conducted additional spatially-resolved experiments at an oven temperature of 723 K in addition to previous data published by Serrer et al. [48] at 623 K. Figure 5 illustrates spatially-resolved CO_2 conversion and selectivity to CH_4 profiles for the catalysts under CO_2 methanation. The catalyst bed starts at a position of 0 mm and ends at 36 mm. Experimental data points are plotted with an error margin of 2.5% based on the accuracy of the GC and errors in spatially measured points.

The temperature profiles reveal a strong hot spot formation in the initial bed zone around 3-9 mm because of the exothermic reaction, leading to a 41% conversion of CO_2 within the hot spot zone. The fact that most of the conversion occurs in the first part of the catalyst bed slows down the reaction in the subsequent part of the catalyst bed, resulting in a decrease in temperature and reaction rate. A small amount of CO is produced at the hot spot through the reverse water-gas shift reaction and is converted to CH_4 along the catalyst bed. The addition of Fe enhances CO_2 methanation at an oven temperature of 623 K, thus producing a higher hot spot temperature and CO_2 conversion than for the monometallic catalysts (Figure 5 (a)). At 623 K, bimetallic catalysts increase the hot spot temperature by 5 K, resulting in 42% CO_2 conversion. Compared with the monometallic catalyst, the bimetallic catalyst exhibits 10% enhanced selectivity towards CH_4 within the hot spot zone at 623 K (Figure 5 (b)).

For both catalysts, 80% CO_2 conversion and 94% CH_4 selectivity were achieved at reactor the exit because the thermodynamic equilibrium is reached.

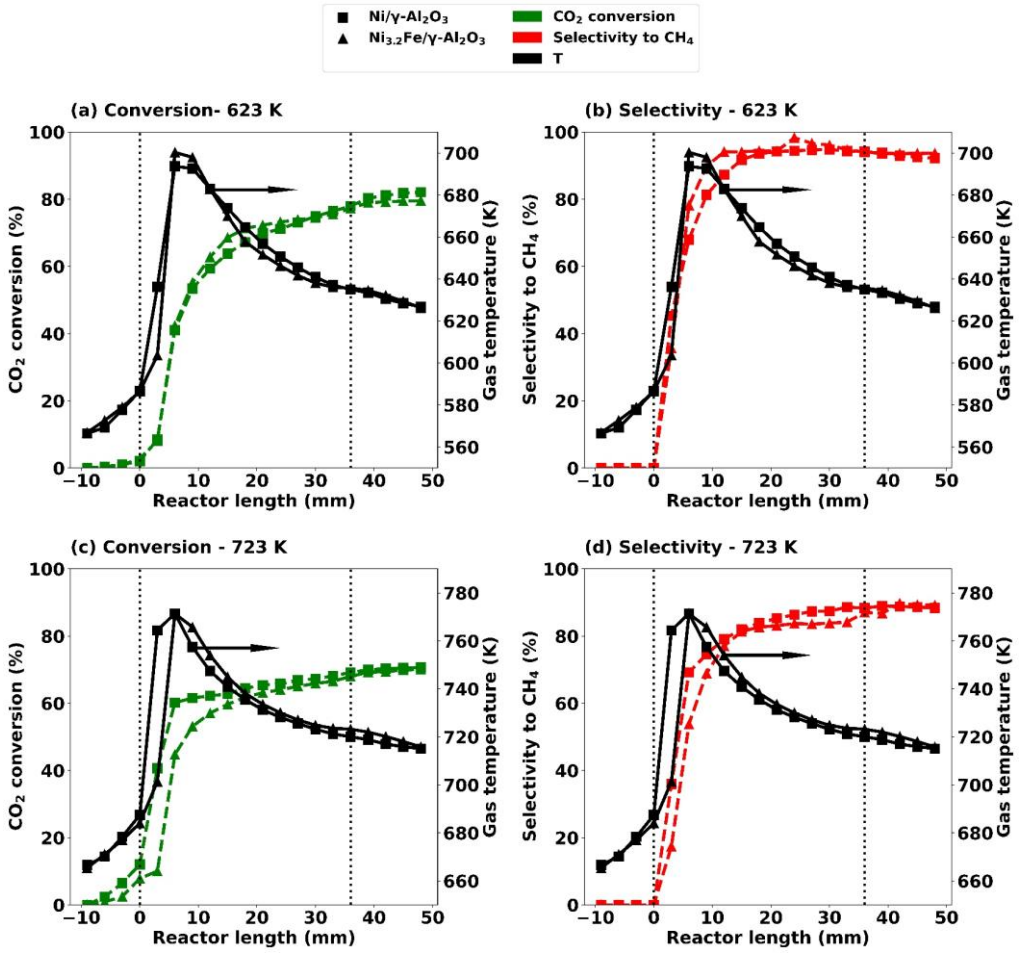

Figure 5: Experimentally obtained spatially-resolved axial profiles of (a) CO_2 conversion at 623 K, (b) selectivity to CH_4 at 623 K, (c) CO_2 conversion at 723 K, and (d) selectivity to CH_4 at 723 K (primary y-axis, left) and temperature (secondary y-axis, right) at an oven temperature of 623 K over 17 wt% Ni/γ-Al_2O_3 and $Ni_{3.2}Fe$/γ-Al_2O_3 catalyst at inlet gas feed composition of 25 vol% of CO_2:H_2 = 1:4 in N_2. Dotted line: bed region (0 mm to 36 mm).

In contrast, CO_2 methanation is not improved by the addition of Fe at an oven temperature of 723 K. Hot spots form earlier with the monometallic catalyst than with bimetallic catalyst (Figure 5 (c)). At a bed length of 3 mm, the hot spot temperature of 764 K was recorded for the monometallic catalyst compared to a temperature of 701 K for the bimetallic catalyst. The monometallic catalyst achieved 60% CO_2 conversion and 69% CH_4 selectivity within the hot spot zone, whereas the bimetallic catalyst showed 45% CO_2 conversion and 54% selectivity for CH_4 (Figure 5 (c) and (d)). Again, both catalysts reach the same conversion at the reactor exit due to thermodynamic equilibrium. This explains also that the CO_2 conversion at an oven temperature of 723 K (≈70%) is lower compared to 623 K (≈80%).

Figure S1 show spatially measured concentration and temperature profile over the Ni/γ-Al_2O_3 or $Ni_{3.2}Fe$/γ-Al_2O_3 catalyst at oven temperature of 623 K and 723 K.

4.4. Modeling results

The thermodynamic consistency of the microkinetic surface reaction scheme proposed by Schmider et al. [42] used in this study was thoroughly evaluated through a comprehensive thermodynamic analysis, as depicted in Figure S2. The unmodified microkinetic model was utilized to simulate both Ni/γ-Al_2O_3 and $Ni_{3.2}Fe$/γ-Al_2O_3 catalyst systems. The active catalytic surface area was considered in the simulations via $F_{cat/geo}$ as described in Eq. (12). Based on measurements, the different $F_{cat/geo}$ values of 103 and 78 were used for Ni/γ-Al_2O_3 and $Ni_{3.2}Fe$/γ-Al_2O_3, respectively.

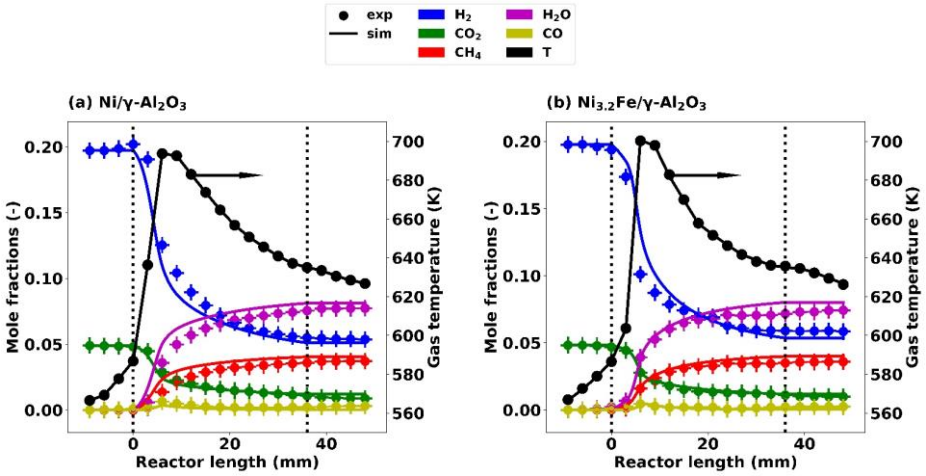

Figure 6: Comparison of experimentally and numerically obtained spatially-resolved mole fractions (primary y-axis, left) and temperature (secondary y-axis, right) profile obtained at an oven temperature of 623 K over (a) 17 wt% Ni/γ-Al_2O_3 and (b) 17 wt% $Ni_{3.2}Fe$/γ-Al_2O_3 catalyst at inlet gas feed composition of 25 vol% of CO_2:H_2 = 1:4 in N_2. Dotted line highlights the bed region (0 mm to 36 mm).

A comparison of experimental and simulated axial mole fraction and temperature profiles during CO_2 methanation over the Ni/γ-Al_2O_3 catalyst is depicted in Figure 6 (a) and over $Ni_{3.2}Fe$/γ-Al_2O_3 in Figure 6 (b) for an oven temperature of 623 K. All species profile show consistent agreement between model prediction and experiment. Additionally, the small amount of CO measured during the experiments is in line with the model predictions. However, in the initial and middle bed zones, there are small deviations between experimental and numerical results. A better agreement is observed during hot zones for bimetallic catalysts compared to monometallic catalysts, which can be explained by different degrees of Ni oxidation, as observed by XAS measurements. As shown in Figure 3 (a), the Ni catalyst oxidizes at an oven temperature of 623 K, resulting in a lower active catalytic surface area. Also, compared to monometallic catalysts, the bimetallic catalysts exhibit a lower oxidation rate of Ni due

to Fe's protective effect (Figure 3 (b)). Consequently, the active surface area of the catalyst changes very little due to Ni oxidation. For the monometallic catalysts, the numerical simulation shows higher conversion compared to the experiments since the present numerical simulation assumes a constant active catalytic area via the $F_{cat/geo}$ parameter. The simulation for the bimetallic catalysts with a constant active catalytic surface area matches the experimental data more closely than for the monometallic catalysts.

An additional study was conducted at an oven temperature of 723 K over shown in Figure 7. The exothermic nature of the Sabatier reaction leads to a decrease in CO_2 conversion and CH_4 selectivity at a higher oven temperature (723 K), as discussed earlier. Moreover, CO formation is increased due to the RWGS reaction. The hot spot moves closer to the bed entrance in comparison to 623 K indicating a faster reaction rate. Both catalysts performed very similarly toward the bed end in terms of CO_2 conversion due to the thermodynamic equilibrium. However, the Ni/Al_2O_3 (Figure 7 (a)) catalyst is found to form hot spots earlier than $Ni_{3.2}Fe/Al_2O_3$ (Figure 7 (b)) catalyst due to its higher activity at 723 K. This result is in agreement with the observation that the addition of Fe at elevated temperatures does not provide a significant promoting effect [20]. Thus, the Ni concentration in a catalyst defines CO_2 methanation activity. In the present study, the monometallic catalyst contains 17 wt% Ni, while the bimetallic catalyst contains 13 wt% Ni. Therefore, the monometallic catalyst with a higher Ni concentration has a higher CO_2 methanation efficiency than the bimetallic catalyst. However, the role of Fe at higher temperatures needs further investigation.

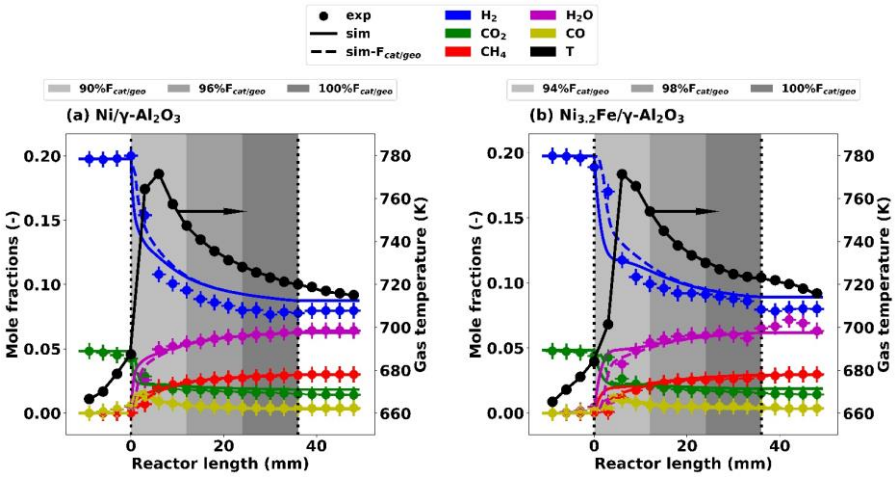

Figure 7: Comparison of experimentally and numerically obtained spatially-resolved mole fractions (primary y-axis, left) and temperature (secondary y-axis, right) profile obtained at an oven temperature of 723 K over (a) 17 wt% $Ni/\gamma\text{-}Al_2O_3$ and (b) 17 wt% $Ni_{3.2}Fe/\gamma\text{-}Al_2O_3$ catalyst at inlet gas feed composition of 25 vol% of CO_2:H_2 = 1:4 in N_2. Dashed line: simulation with variable catalytic surface area. The solid line represents the simulation with constant catalytic surface area.

As a next step, for a more rigorous description of the catalyst under operating conditions, we included the structural information of the catalyst (i.e. oxidation state) in the simulation studies to fully comprehend the CO_2 methanation. Based on the XAS measurements, simulations are performed in the following section by incorporating the oxidation state of Ni. To achieve this, the catalyst bed was divided into three equal sections, each with a different catalytic surface area, where the $F_{cat/geo}$ parameter is varied along the reactor bed based on XAS data. Therefore, the bed was divided equally into three sections for the second set of simulations, shown in Figure 7 by the highlighted region (dashed line). Figure S3 and S4 compare simulations and experiments at 623 K for Ni/γ-Al_2O_3 and $Ni_{3.2}$Fe/γ-Al_2O_3 catalysts, showing the impact of changing catalytic surface area. The simulations were performed by varying the Fcat/geo value in the first two regions of the catalyst bed, i.e. 0 mm to 12 mm and 12 mm to 24 mm, while retaining the measured value for the last region. At 723 K, for Ni/γ-Al_2O_3 catalyst, the $F_{cat/geo}$ values are 92.7 (0 mm to 12), 98.9 (12 mm to 24 mm), and 103.0 (24 mm to 36 mm) (Figure 7 (a) highlighted region). For the $Ni_{3.2}$Fe/γ-Al_2O_3 catalyst, the $F_{cat/geo}$ values are 73.3, 76.4, and 78 (Figure 7 (b) highlighted region).

Comparing simulated and experimental results in the axial direction of the catalyst bed reveals deviations during hot spot, as shown in Figure 7 (solid line). The Ni catalyst tends to be slightly oxidized in the initial (hot spot) and middle region of the catalyst bed (shown in Figure 3) [48]. The XAS results indicate that almost 0.5-1.5% of Ni undergo oxidation at 623 K. It was reported that 7-9% Ni oxidation was observed for monometallic catalysts in contrast to 4-6% for bimetallic catalysts at 723 K [48]. The results indicate that either FeO_x species clean Ni surfaces of oxygen, or dissociative CO_2 activation occurs at FeO_x centers. As a result, combined XAS and CO_2-TPO studies suggest increased Ni oxidation at an increase in hot spot temperature. In the simulations, the change in oxidation state can be accommodated by adjusting the active catalytic surface area via the model parameter $F_{cat/geo}$ from the measured value for a completely reduced catalyst (dashed line, Figure 7). The inclusion of oxidation in the microkinetic model enables a considerable improvement in the agreement between simulation and experiment. Yet, there are still some differences between numerical and experimental results. The difference between the two lies primarily in the first 12 mm of the catalyst bed, where most oxidation occurs. There is an overestimation of the numerical prediction since oxidation is a continuous function of axial position instead of a discrete function. Further, limited heat transfer can also account for the additional differences because grains themselves may be hotter than thermocouple measurements.

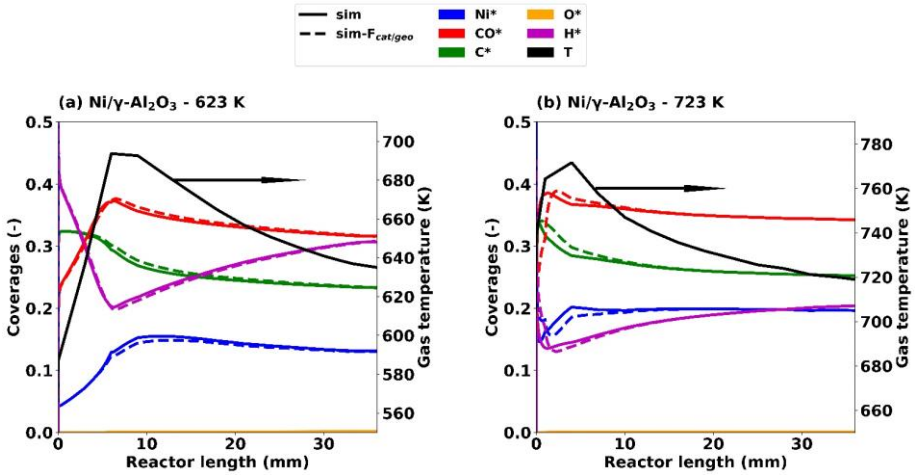

Figure 8: Numerically obtained spatially-resolved surface coverage (primary y axis, left) and temperature (secondary y axis, right) profile of 17 wt% Ni/γ-Al_2O_3 catalyst at inlet gas feed of 25 vol% of CO_2:H_2 = 1:4 in N_2 only in bed region (0 mm to 36 mm). Solid line: simulations with constant catalytic surface area; dashed line: simulations with varied catalytic surface area.

Comparative analysis is performed between the predicted surface coverage profiles at an oven temperature of 623 K and 723 K, shown in Figure 8. Figure 8 (b) shows a comparison of the constant and varied catalytic surface areas at 723 K. The microkinetics used in the present study were developed for CO_2 methanation on a Ni catalyst. Therefore, Fe is not considered. As a result, only the fractional surface coverages over the Ni surface are shown in Figure 8. The microkinetic model predicts coke formation by including C* as an active intermediate species. At 623 K and 723 K, the profile shows that the catalyst is primarily covered with CO*, C* and H*. Simulation results indicate CO* coverage of 37% and 38% and C* coverage is 32% and 34% at an oven temperature of 623 K and 723 K, respectively. The high CO* coverage predicted by the model is consistent with DRIFTS measurements and the literature [52,93,94]. At 723 K, the higher activity of Ni causes hot spots to form earlier in the catalyst bed. This results in an earlier decline in the H* profile compared to 623 K. Additionally, a small fraction of H* is present at 623 K and 723 K due to CO formation during RWGS reaction, shown in Figure 6 and Figure 7. As the CO formation takes place rapidly in the hot spot zone, the CO* coverage fraction increases. Downstream of the hot spot, CO* decreases more slowly at 723 K oven temperature compared with 623 K. This decrease in CO* allows more Ni* to be available, increasing the adsorption of H*, which then reacts with CO_2 to form CH_4. At 723 K, the lower H*/CO* ratio on the catalyst surface causes a decrease in CH_4 selectivity. The species coverage shows only a slight difference when the catalytic surface area is varied at 723 K (Figure 8 (b)). Under all conditions, simulation results indicate that O* coverage is below 0.5%. Oxidation usually occurs at the step and edge sites, which is not covered by the present microkinetic model.

The approach presented in this study enhances modeling predictions by incorporating catalyst structural information. This model opens up exciting possibilities for multiscale modeling to achieve accurate predictions of hot-spots, improved reactor design, optimized heat management, and successful scale-up. To take the predictions to the next level, a more comprehensive, first principles-based description that considers the actual shape of catalytic particles is necessary [86,89,95,96].

5. Conclusion

CO_2 methanation over Ni based catalysts was studied experimentally and numerically. In the spatially-resolved experiments over 17 wt% Ni/γ-Al_2O_3 and 17 wt% $Ni_{3.2}Fe$/γ-Al_2O_3 catalysts at an oven temperature of 623 K and 723 K, it was observed that strong concentration and temperature gradients formed along the catalyst bed, affecting catalyst structure and causing catalyst oxidation. The model approach uses a 1D packed-bed reactor model with detailed microkinetics and mass transfer. The predictions of the model are compared with axially-resolved concentration gradients and temperature profiles for CO_2 methanation. Spatially-resolved structural information from synchrotron-based *operando* QEXAFS measurements and surface species analyzed by DRIFTS measurements recorded at different temperatures were used to understand the impact of spatial variation of the active catalytic surface area in operation. These effects were then incorporated in the formulation of catalysts' conditions of the model approach.

Simulated and experimental spatial profiles were in reasonable agreement at 623 K for both catalysts. However, visible deviations from experimental results in the hot spot area were observed at 723 K. *Operando* XAS revealed catalyst oxidation at the inlet and in the middle of the catalyst bed under CO_2 methanation conditions leading to a decrease in active surface area. The simulations were shown to be improved by varying the active catalytic surface area based on *operando* XAS data to mimic the oxidation degree. This demonstrates the importance of taking oxidation of the active site or, in general, the structural change of the active site motif into account in microkinetic models through a combination of *operando* experiments and ab-initio calculations. As a final conclusion, we can state that combination of microkinetic modeling that also account for oxidation states lea to much better understanding of intrinsic kinetics.

Acknowledgement

The omegadot software & consulting GmbH is gratefully acknowledged for a cost-free academic license of DETCHEM. The authors would like to thank Rinu Chacko, Hendrik Goßler, Sofia Angeli, and Erisa Saraçi (all KIT) for fruitful discussions. We further acknowledge Marc-André Serrer (KIT) and Matthias Stehle (KIT) for conducting and supporting spatially-resolved profile measurents, DRIFTS and

XAS experiments. We thank the X10DA (SuperXAS) beamline, Maarten Nachtegaal (PSI), Olga Safonova (PSI) and Adam Hugh Clark (PSI) at the Swiss Light Source (SLS) in Villigen (Switzerland) for providing beamtime and support during experiments. Further, we gratefully acknowledge Henning Lichtenberg, Charlotte Fritsch and Florian Maurer for beamtime support. The German Federal Ministry of Education and Research (BMBF) is gratefully acknowledged for financial support within the Kopernikus Project P2X and, further, we thank the SPP2080 (DFG-priority program, GR 3987/13-1 and 14-1) as well as SFB 1441 (B4), project 426888090, all for financial support and a discussion forum for "Catalysts and reactors under dynamic conditions for energy storage and conversion". We acknowledge the Helmholtz Research Programs METE and STN for financial support, latter one related to laser drilling of the glass capillaries.

Supporting Information Available

The correlations and equations used for the calculation of fluid-solid mass transfer, energy balance, and diffusion coefficient are provided in supplementary material. Also, the table of parameters used for simulation, experimentally measured spatially-resolved temperature and concentration profiles, thermodynamic analysis, and comparison of experimental and numerical simulation with variable catalytic surface area at 623 K are given in the supplementary material.

Abbreviations

XAS	X-ray absorption spectroscopy
QEXAFS	Quick scanning extended X-ray absorption fine structure
XANES	X-ray near edge absorption spectra
DRIFTS	Diffuse reflectance infrared Fourier transform spectroscopy
ICP-OES	Inductively coupled plasma optical emission spectroscopy
STEM	Scanning transmission electron microscopy
GC	Gas chromatography
MS	Mass spectrometer

PBR	Packed-bed reactor

534 # List of symbols

Latin symbols

A	Pre-exponential factor	s^{-1}
A_{cat}	Microscopic area provided by the active catalyst for the catalytic reaction	m^2
A_{geo}	Microscopic area of the gas-phase surface interface of the particles	m^2
a_{v}	Ratio of particle surface area to reactor volume	m^{-1}
c_{p}	Specific heat capacity at constant pressure	J kg^{-1} k^{-1}
c_i	Concentration of adsorbed species or gas-phase species i	mol m^{-2} or mol m^{-3}
D	Dispersion	-
D_{eff}	Effective diffusion coefficient	m^2 s^{-1}
D_{knud}	Knudsen diffusion coefficient	m^2 s^{-1}
D_{mol}	Molecular diffusion coefficient	m^2 s^{-1}
d_{t}	Diameter of reactor tube	m
d_{p}	Particle diameter	m
d_{pore}	Pore diameter of particle	m
E_{a}	Activation energy	kJ mol^{-1}
$F_{\mathrm{cat/geo}}$	Active catalytic surface area to the geometric surface area of the catalyst particle	-

f	Friction factor	-
h	Specific enthalpy	J mol^{-1}
h_{fs}	Fluid-solid mass transfer coefficient	W m^{-2} K^{-1}
k	Rate constant	s^{-1}
k_{eff}	Effective rate constant	s^{-1}
k_{fs}	Fluid-solid mass transfer coefficient	m s^{-1}
M	Molar mass	kg mol^{-1}
Nu	Nusselt number	-
n_{cat}	Molar amount of active catalyst	mol
Pr	Prandtl number	-
p	Pressure	Pa
R	Universal gas constant	J mol^{-1} K^{-1}
R^{surf}	Effective molar production of rate of gas-phase species by surface reaction	mol m^{-2} s^{-1}
Re	Reynolds number	-
R_{s}	Set of surface reactions	-
Sh	Sherwood number	-
Sc	Schmidt number	-
S_{g}	Set of gas-phase species	-
S_{s}	Set of surface species	-
$\dot{s}$	Molar production rate of gas-phase species by surface reaction	mol m^{-2} s^{-1}

T	Gas-phase temperature	K
T_{s}	Solid-phase temperature	K
T_{w}	Reactor wall temperature	K
U	Overall heat transfer coefficient	W m^{-2} K^{-1}
u	Superficial velocity of gas	m s^{-1}
Y	Mass faction of gas-phase specie	-
z	Reactor axial coordinate	m

Greek symbols

β	Temperature dependency parameter	-
Γ_{cat}	Surface site density of active catalyst surface area	mol m^{-2}
ε	Bed porosity	-
ε_{p}	Porosity of particle	-
ϵ	Coverage dependency of the activation energy	kJ mol^{-1}
η	Effectiveness factor	-
θ	Fractional surface coverage of species	-
λ	Thermal conductivity	W m^{-1} K^{-1}
μ	Gas mixture viscosity	kg m^{-1} s^{-1}
ν	Stoichiometric coefficients	-
ρ	Gas mixture density	kg m^{-3}
σ	Number of sites occupied by the one particle of the species	-

τ_p	Tortuosity of particle	-
ϕ	Thiele modulus	-

References

[1] C. Le Quéré, M.R. Raupach, J.G. Canadell, G. Marland, L. Bopp, P. Ciais, T.J. Conway, S.C. Doney, R.A. Feely, P. Foster, P. Friedlingstein, K. Gurney, R.A. Houghton, J.I. House, C. Huntingford, P.E. Levy, M.R. Lomas, J. Majkut, N. Metzl, J.P. Ometto, G.P. Peters, I.C. Prentice, J.T. Randerson, S.W. Running, J.L. Sarmiento, U. Schuster, S. Sitch, T. Takahashi, N. Viovy, G.R. van der Werf, F.I. Woodward, Trends in the sources and sinks of carbon dioxide, Nat. Geosci. 2 (2009) 831–836. https://doi.org/10.1038/ngeo689.

[2] C. Song, Global challenges and strategies for control, conversion and utilization of CO2 for sustainable development involving energy, catalysis, adsorption and chemical processing, Catal. Today. 115 (2006) 2–32. https://doi.org/10.1016/j.cattod.2006.02.029.

[3] J. Ma, N. Sun, X. Zhang, N. Zhao, F. Xiao, W. Wei, Y. Sun, A short review of catalysis for CO2 conversion, Catal. Today. 148 (2009) 221–231. https://doi.org/10.1016/j.cattod.2009.08.015.

[4] W. Wang, S. Wang, X. Ma, J. Gong, Recent advances in catalytic hydrogenation of carbon dioxide, Chem. Soc. Rev. 40 (2011) 3703–3727. https://doi.org/10.1039/C1CS15008A.

[5] Z. Jiang, T. Xiao, V.L. Kuznetsov, P.P. Edwards, Turning carbon dioxide into fuel, Philos. Trans. R. Soc. A Math. Phys. Eng. Sci. 368 (2010) 3343–3364. https://doi.org/10.1098/rsta.2010.0119.

[6] T. Sakakura, J.-C. Choi, H. Yasuda, Transformation of Carbon Dioxide, Chem. Rev. 107 (2007) 2365–2387. https://doi.org/10.1021/cr068357u.

[7] V. Menon, V.M. Janardhanan, O. Deutschmann, A mathematical model to analyze solid oxide electrolyzer cells (SOECs) for hydrogen production, Chem. Eng. Sci. 110 (2014) 83–93. https://doi.org/10.1016/j.ces.2013.10.025.

[8] W.L. Vrijburg, E. Moioli, W. Chen, M. Zhang, B.J.P. Terlingen, B. Zijlstra, I.A.W. Filot, A. Züttel, E.A. Pidko, E.J.M. Hensen, Efficient Base-Metal NiMn/TiO2 Catalyst for CO2 Methanation, ACS Catal. 9 (2019) 7823–7839. https://doi.org/10.1021/acscatal.9b01968.

[9] K.F. Kalz, R. Kraehnert, M. Dvoyashkin, R. Dittmeyer, R. Gläser, U. Krewer, K. Reuter, J.-D. Grunwaldt, Future Challenges in Heterogeneous Catalysis: Understanding Catalysts under Dynamic Reaction Conditions, ChemCatChem. 9 (2017) 17–29.

https://doi.org/10.1002/cctc.201600996.

[10] A.I. Tsiotsias, N.D. Charisiou, I. V Yentekakis, M.A. Goula, Bimetallic ni-based catalysts for CO2 methanation: A review, Nanomaterials. 11 (2020) 28. https://doi.org/10.3390/nano11010028.

[11] M. Thema, F. Bauer, M. Sterner, Power-to-Gas: Electrolysis and methanation status review, Renew. Sustain. Energy Rev. 112 (2019) 775–787. https://doi.org/10.1016/j.rser.2019.06.030.

[12] M. Jentsch, T. Trost, M. Sterner, Optimal use of power-to-gas energy storage systems in an 85% renewable energy scenario, Energy Procedia. 46 (2014) 254–261. https://doi.org/10.1016/j.egypro.2014.01.180.

[13] P. Sabatier, J.B. Senderens, Direct hydrogenation of oxides of carbon in presence of various finely divided metals, CR Acad Sci. 134 (1902) 689–691.

[14] J. Gao, Q. Liu, F. Gu, B. Liu, Z. Zhong, F. Su, Recent advances in methanation catalysts for the production of synthetic natural gas, Rsc Adv. 5 (2015) 22759–22776. https://doi.org/10.1039/C4RA16114A.

[15] M.A.A. Aziz, A.A. Jalil, S. Triwahyono, A. Ahmad, CO2 methanation over heterogeneous catalysts: recent progress and future prospects, Green Chem. 17 (2015) 2647–2663. https://doi.org/10.1039/C5GC00119F.

[16] J.N. Park, E.W. McFarland, A highly dispersed Pd-Mg/SiO2 catalyst active for methanation of CO2, J. Catal. 266 (2009) 92–97. https://doi.org/10.1016/j.jcat.2009.05.018.

[17] F. Ocampo, B. Louis, L. Kiwi-Minsker, A.-C. Roger, Effect of Ce/Zr composition and noble metal promotion on nickel based CexZr1− xO2 catalysts for carbon dioxide methanation, Appl. Catal. A Gen. 392 (2011) 36–44. https://doi.org/10.1016/j.apcata.2010.10.025.

[18] J. Ashok, M.L. Ang, S. Kawi, Enhanced activity of CO2 methanation over Ni/CeO2-ZrO2 catalysts: Influence of preparation methods, Catal. Today. 281 (2017) 304–311. https://doi.org/10.1016/j.cattod.2016.07.020.

[19] G. Garbarino, P. Riani, L. Magistri, G. Busca, A study of the methanation of carbon dioxide on Ni/Al2O3 catalysts at atmospheric pressure, Int. J. Hydrogen Energy. 39 (2014) 11557–11565. https://doi.org/10.1016/j.ijhydene.2014.05.111.

[20] B. Mutz, M. Belimov, W. Wang, P. Sprenger, M.A. Serrer, D. Wang, P. Pfeifer, W. Kleist, J.-D. Grunwaldt, Potential of an alumina-supported Ni3Fe catalyst in the methanation of CO2:

593 Impact of alloy formation on activity and stability, ACS Catal. 7 (2017) 6802–6814.
594 https://doi.org/10.1021/acscatal.7b01896.

595 [21] N.D. Charisiou, L. Tzounis, V. Sebastian, S.J. Hinder, M.A. Baker, K. Polychronopoulou, M.A.
596 Goula, Investigating the correlation between deactivation and the carbon deposited on the
597 surface of Ni/Al2O3 and Ni/La2O3-Al2O3 catalysts during the biogas reforming reaction, Appl.
598 Surf. Sci. 474 (2019) 42–56. https://doi.org/10.1016/j.apsusc.2018.05.177.

599 [22] K.N. Papageridis, N.D. Charisiou, S. Douvartzides, V. Sebastian, S.J. Hinder, M.A. Baker, S.
600 AlKhoori, K. Polychronopoulou, M.A. Goula, Promoting effect of CaO-MgO mixed oxide on
601 Ni/γ-Al2O3 catalyst for selective catalytic deoxygenation of palm oil, Renew. Energy. 162
602 (2020) 1793–1810. https://doi.org/10.1016/j.renene.2020.09.133.

603 [23] B. Mutz, H.W.P. de Carvalho, W. Kleist, J.-D. Grunwaldt, Dynamic transformation of small Ni
604 particles during methanation of CO2 under fluctuating reaction conditions monitored by
605 operando X-ray absorption spectroscopy, J. Phys. Conf. Ser. 712 (2016) 12050.
606 https://doi.org/10.1088/1742-6596/712/1/012050.

607 [24] B. Kreitz, A. Martínez Arias, J. Martin, A.P. Weber, T. Turek, Spray-Dried Ni Catalysts with
608 Tailored Properties for CO2 Methanation, Catalysts. 10 (2020).
609 https://doi.org/10.3390/catal10121410.

610 [25] L. Foppa, T. Margossian, S.M. Kim, C. Müller, C. Copéret, K. Larmier, A. Comas-Vives,
611 Contrasting the Role of Ni/Al2O3 Interfaces in Water–Gas Shift and Dry Reforming of
612 Methane, J. Am. Chem. Soc. 139 (2017) 17128–17139. https://doi.org/10.1021/jacs.7b08984.

613 [26] Q. Pan, J. Peng, T. Sun, S. Wang, S. Wang, Insight into the reaction route of CO2 methanation:
614 Promotion effect of medium basic sites, Catal. Commun. 45 (2014) 74–78.
615 https://doi.org/10.1016/j.catcom.2013.10.034.

616 [27] D. Pandey, G. Deo, Effect of support on the catalytic activity of supported Ni-Fe catalysts for
617 the CO2 methanation reaction, J. Ind. Eng. Chem. 33 (2016) 99–107.
618 https://doi.org/10.1016/j.jiec.2015.09.019.

619 [28] B. Mutz, P. Sprenger, W. Wang, D. Wang, W. Kleist, J.-D. Grunwaldt, Operando Raman
620 spectroscopy on CO2 methanation over alumina-supported Ni, Ni3Fe and NiRh0.1 catalysts:
621 Role of carbon formation as possible deactivation pathway, Appl. Catal. A Gen. 556 (2018)
622 160–171. https://doi.org/10.1016/j.apcata.2018.01.026.

623 [29] B. Mutz, A.M. Gänzler, M. Nachtegaal, O. Müller, R. Frahm, W. Kleist, J.-D. Grunwaldt, Surface

624 oxidation of supported Ni particles and its impact on the catalytic performance during
625 dynamically operated methanation of CO2, Catalysts. 7 (2017) 279.
626 https://doi.org/10.3390/catal7090279.

627 [30] C. Vogt, E. Groeneveld, G. Kamsma, M. Nachtegaal, L. Lu, C.J. Kiely, P.H. Berben, F. Meirer,
628 B.M. Weckhuysen, Unravelling structure sensitivity in CO2 hydrogenation over nickel, Nat.
629 Catal. 1 (2018) 127–134. https://doi.org/10.1038/s41929-017-0016-y.

630 [31] C. Vogt, M. Monai, E.B. Sterk, J. Palle, A.E.M. Melcherts, B. Zijlstra, E. Groeneveld, P.H.
631 Berben, J.M. Boereboom, E.J.M. Hensen, Understanding carbon dioxide activation and
632 carbon–carbon coupling over nickel, Nat. Commun. 10 (2019) 1–10.
633 https://doi.org/10.1038/s41467-019-12858-3.

634 [32] B. Kreitz, G.D. Wehinger, C.F. Goldsmith, T. Turek, Microkinetic modeling of the transient CO2
635 methanation with DFT-based uncertainties in a Berty reactor, ChemCatChem. (2022).
636 https://doi.org/10.1002/cctc.202200570.

637 [33] T. Burger, S. Ewald, A. Niederdränk, F.E. Wagner, K. Köhler, O. Hinrichsen, Enhanced activity
638 of co-precipitated NiFeAlOx in CO2 methanation by segregation and oxidation of Fe, Appl.
639 Catal. A Gen. 604 (2020) 117778. https://doi.org/10.1016/j.apcata.2020.117778.

640 [34] C. Mebrahtu, F. Krebs, S. Abate, S. Perathoner, G. Centi, R. Palkovits, CO2 Methanation:
641 Principles and Challenges, in: S. Albonetti, S. Perathoner, E.A.B.T.-S. in S.S. and C. Quadrelli
642 (Eds.), Stud. Surf. Sci. Catal., Elsevier, 2019: pp. 85–103. https://doi.org/10.1016/B978-0-444-
643 64127-4.00005-7.

644 [35] A.L. Kustov, A.M. Frey, K.E. Larsen, T. Johannessen, J.K. Nørskov, C.H. Christensen, CO
645 methanation over supported bimetallic Ni–Fe catalysts: From computational studies towards
646 catalyst optimization, Appl. Catal. A Gen. 320 (2007) 98–104.
647 https://doi.org/10.1016/j.apcata.2006.12.017.

648 [36] M.A. Serrer, A. Gaur, J. Jelic, S. Weber, C. Fritsch, A.H. Clark, E. Saraçi, F. Studt, J.-D.
649 Grunwaldt, Structural dynamics in Ni-Fe catalysts during CO2 methanation-role of iron oxide
650 clusters, Catal. Sci. Technol. 10 (2020) 7542–7554. https://doi.org/10.1039/d0cy01396j.

651 [37] L.R. Winter, E. Gomez, B. Yan, S. Yao, J.G. Chen, Tuning Ni-catalyzed CO2 hydrogenation
652 selectivity via Ni-ceria support interactions and Ni-Fe bimetallic formation, Appl. Catal. B
653 Environ. 224 (2018) 442–450. https://doi.org/10.1016/j.apcatb.2017.10.036.

654 [38] G. Giorgianni, C. Mebrahtu, M.E. Schuster, A.I. Large, G. Held, P. Ferrer, F. Venturini, D.

655 Grinter, R. Palkovits, S. Perathoner, Elucidating the mechanism of the CO 2 methanation
656 reaction over Ni–Fe hydrotalcite-derived catalysts via surface-sensitive in situ XPS and
657 NEXAFS, Phys. Chem. Chem. Phys. 22 (2020) 18788–18797.
658 https://doi.org/10.1039/D0CP00622J.

659 [39] B. Yan, B. Zhao, S. Kattel, Q. Wu, S. Yao, D. Su, J.G. Chen, Tuning CO2 hydrogenation
660 selectivity via metal-oxide interfacial sites, J. Catal. 374 (2019) 60–71.
661 https://doi.org/10.1016/j.jcat.2019.04.036.

662 [40] T. Schaaf, J. Grünig, M.R. Schuster, T. Rothenfluh, A. Orth, Methanation of CO2-storage of
663 renewable energy in a gas distribution system, Energy. Sustain. Soc. 4 (2014) 1–14.
664 https://doi.org/10.1186/s13705-014-0029-1.

665 [41] S. Rönsch, J. Schneider, S. Matthischke, M. Schlüter, M. Götz, J. Lefebvre, P. Prabhakaran, S.
666 Bajohr, Review on methanation–From fundamentals to current projects, Fuel. 166 (2016)
667 276–296. https://doi.org/10.1016/j.fuel.2015.10.111.

668 [42] D. Schmider, L. Maier, O. Deutschmann, Reaction Kinetics of CO and CO2 Methanation over
669 Nickel, Ind. Eng. Chem. Res. 60 (2021) 5792–5805. https://doi.org/10.1021/acs.iecr.1c00389.

670 [43] J. Gao, Y. Wang, Y. Ping, D. Hu, G. Xu, F. Gu, F. Su, A thermodynamic analysis of methanation
671 reactions of carbon oxides for the production of synthetic natural gas, RSC Adv. 2 (2012)
672 2358–2368. https://doi.org/10.1039/C2RA00632D.

673 [44] A. Urakawa, N. Maeda, A. Baiker, Space- and Time-Resolved Combined DRIFT and Raman
674 Spectroscopy: Monitoring Dynamic Surface and Bulk Processes during NOx Storage
675 Reduction, Angew. Chemie Int. Ed. 47 (2008) 9256–9259.
676 https://doi.org/10.1002/anie.200804077.

677 [45] T. Hyakutake, W. van Beek, A. Urakawa, Unravelling the nature, evolution and spatial
678 gradients of active species and active sites in the catalyst bed of unpromoted and K/Ba-
679 promoted Cu/Al 2 O 3 during CO 2 capture-reduction, J. Mater. Chem. A. 4 (2016) 6878–6885.
680 https://doi.org/10.1039/C5TA09461E.

681 [46] A.M. Gänzler, M. Casapu, A. Boubnov, O. Müller, S. Conrad, H. Lichtenberg, R. Frahm, J.-D.
682 Grunwaldt, Operando spatially and time-resolved X-ray absorption spectroscopy and infrared
683 thermography during oscillatory CO oxidation, J. Catal. 328 (2015) 216–224.
684 https://doi.org/10.1016/j.jcat.2015.01.002.

685 [47] M. Geske, O. Korup, R. Horn, Resolving kinetics and dynamics of a catalytic reaction inside a

fixed bed reactor by combined kinetic and spectroscopic profiling, Catal. Sci. Technol. 3 (2013) 169–175. https://doi.org/10.1039/C2CY20489D.

[48] M.A. Serrer, M. Stehle, M.L. Schulte, H. Besser, W. Pfleging, E. Saraçi, J.-D. Grunwaldt, Spatially-Resolved Insights Into Local Activity and Structure of Ni-Based CO2 Methanation Catalysts in Fixed-Bed Reactors, ChemCatChem. 13 (2021) 3010–3020. https://doi.org/10.1002/cctc.202100490.

[49] D. Schlereth, O. Hinrichsen, A fixed-bed reactor modeling study on the methanation of CO2, Chem. Eng. Res. Des. 92 (2014) 702–712. https://doi.org/10.1016/j.cherd.2013.11.014.

[50] B. Kreitz, G.D. Wehinger, T. Turek, Dynamic simulation of the CO2 methanation in a micro-structured fixed-bed reactor, Chem. Eng. Sci. 195 (2019) 541–552. https://doi.org/10.1016/j.ces.2018.09.053.

[51] J. Bremer, K. Sundmacher, Operation range extension via hot-spot control for catalytic CO2 methanation reactors, React. Chem. Eng. 4 (2019) 1019–1037. https://doi.org/10.1039/C9RE00147F.

[52] B. Kreitz, K. Sargsyan, K. Blöndal, E.J. Mazeau, R.H. West, G.D. Wehinger, T. Turek, C.F. Goldsmith, Quantifying the impact of parametric uncertainty on automatic mechanism generation for CO2 hydrogenation on Ni (111), JACS Au. 1 (2021) 1656–1673. https://doi.org/10.1021/jacsau.1c00276.

[53] R. Kumar, D. Marais, N. Variations, Methanation and photo-methanation of carbon dioxide at room temperature and atmospheric pressure, Lett. Nat. (1987) 17–19.

[54] H.L. Huynh, J. Zhu, G. Zhang, Y. Shen, W.M. Tucho, Y. Ding, Z. Yu, Promoting effect of Fe on supported Ni catalysts in CO2 methanation by in situ DRIFTS and DFT study, J. Catal. 392 (2020) 266–277. https://doi.org/10.1016/j.jcat.2020.10.018.

[55] M.P. Andersson, T. Bligaard, A. Kustov, K.E. Larsen, J. Greeley, T. Johannessen, C.H. Christensen, J.K. Nørskov, Toward computational screening in heterogeneous catalysis: Pareto-optimal methanation catalysts, J. Catal. 239 (2006) 501–506. https://doi.org/10.1016/j.jcat.2006.02.016.

[56] K.A. Layman, M.E. Bussell, Infrared spectroscopic investigation of CO adsorption on silica-supported nickel phosphide catalysts, J. Phys. Chem. B. 108 (2004) 10930–10941. https://doi.org/10.1021/jp037101e.

[57] S. Farsi, W. Olbrich, P. Pfeifer, R. Dittmeyer, A consecutive methanation scheme for

717 conversion of CO2 – A study on Ni3Fe catalyst in a short-contact time micro packed bed
718 reactor, Chem. Eng. J. 388 (2020) 124233. https://doi.org/10.1016/j.cej.2020.124233.

719 [58] V.A. Danilov, M. Wichert, G. Kolb, 2D model of the transfer processes for CO2 methanation in
720 a microchannel reactor, Chem. Eng. J. 450 (2022) 137863.
721 https://doi.org/10.1016/j.cej.2022.137863.

722 [59] F. Vidal Vázquez, J. Kihlman, A. Mylvaganam, P. Simell, M.L. Koskinen-Soivi, V. Alopaeus,
723 Modeling of nickel-based hydrotalcite catalyst coated on heat exchanger reactors for CO2
724 methanation, Chem. Eng. J. 349 (2018) 694–707. https://doi.org/10.1016/j.cej.2018.05.119.

725 [60] L. Li, W. Zeng, M. Song, X. Wu, G. Li, C. Hu, Research Progress and Reaction Mechanism of
726 CO2 Methanation over Ni-Based Catalysts at Low Temperature: A Review, Catalysts. 12
727 (2022). https://doi.org/10.3390/catal12020244.

728 [61] J. Kopyscinski, T.J. Schildhauer, S.M.A. Biollaz, Production of synthetic natural gas (SNG) from
729 coal and dry biomass - A technology review from 1950 to 2009, Fuel. 89 (2010) 1763–1783.
730 https://doi.org/10.1016/j.fuel.2010.01.027.

731 [62] M. Sudiro, A. Bertucco, G. Groppi, E. Tronconi, Simulation of a structured catalytic reactor for
732 exothermic methanation reactions producing synthetic natural gas, in: S. Pierucci, G.B.B.T.-
733 C.A.C.E. Ferraris (Eds.), Comput. Aided Chem. Eng., Elsevier, 2010: pp. 691–696.
734 https://doi.org/10.1016/S1570-7946(10)28116-6.

735 [63] L. Kiewidt, J. Thöming, Predicting optimal temperature profiles in single-stage fixed-bed
736 reactors for CO2-methanation, Chem. Eng. Sci. 132 (2015) 59–71.
737 https://doi.org/10.1016/j.ces.2015.03.068.

738 [64] T. Eppinger, K. Seidler, M. Kraume, DEM-CFD simulations of fixed bed reactors with small
739 tube to particle diameter ratios, Chem. Eng. J. 166 (2011) 324–331.
740 https://doi.org/10.1016/j.cej.2010.10.053.

741 [65] A.G. Dixon, M. Nijemeisland, CFD as a Design Tool for Fixed-Bed Reactors, Ind. Eng. Chem.
742 Res. 40 (2001) 5246–5254. https://doi.org/10.1021/ie001035a.

743 [66] G.D. Wehinger, B. Kreitz, C.F. Goldsmith, Non-Idealities in Lab-Scale Kinetic Testing: A
744 Theoretical Study of a Modular Temkin Reactor, Catalysts. 12 (2022).
745 https://doi.org/10.3390/catal12030349.

746 [67] E.A. Daymo, M. Hettel, O. Deutschmann, G.D. Wehinger, Accelerating particle-resolved CFD
747 simulations of catalytic fixed-bed reactors with DUO, Chem. Eng. Sci. 250 (2022) 117408.

748 https://doi.org/10.1016/j.ces.2021.117408.

749 [68] J.-D. Grunwaldt, M. Caravati, S. Hannemann, A. Baiker, X-ray absorption spectroscopy under
750 reaction conditions: suitability of different reaction cells for combined catalyst
751 characterization and time-resolved studies, Phys. Chem. Chem. Phys. 6 (2004) 3037–3047.
752 https://doi.org/10.1039/B403071K.

753 [69] J.-D. Grunwaldt, N. Van Vegten, A. Baiker, Insight into the structure of supported palladium
754 catalysts during the total oxidation of methane, Chem. Commun. (2007) 4635–4637.
755 https://doi.org/10.1039/b710222d.

756 [70] R. Frahm, New method for time dependent x-ray absorption studies, Rev. Sci. Instrum. 60
757 (1989) 2515–2518. https://doi.org/10.1063/1.1140716.

758 [71] S. Wan, K. Keller, P. Lott, A.B. Shirsath, S. Tischer, T. Häber, R. Suntz, O. Deutschmann,
759 Experimental and numerical investigation of NO oxidation on Pt/Al2O3- and NOx storage on
760 Pt/BaO/Al2O3-catalysts, Catal. Sci. Technol. (2022). https://doi.org/10.1039/d2cy00572g.

761 [72] R.E. Hayes, P.K. Mok, J. Mmbaga, M. Votsmeier, A fast approximation method for computing
762 effectiveness factors with non-linear kinetics, Chem. Eng. Sci. 62 (2007) 2209–2215.
763 https://doi.org/10.1016/j.ces.2007.01.018.

764 [73] O. Deutschmann, S. Tischer, S. Kleditzsch, V. Janardhanan, C. Correa, D. Chatterjee, N.
765 Mladenov, H.D. Minh, H. Karadeniz, M. Hettel, V. Menon, A. Banerjee, H. Gossler, A. Shirsath,
766 E. Daymo, DETCHEM, (2022). http://www.detchem.com.

767 [74] V. Gnielinski, G9 Fluid-Particle Heat Transfer in Flow Through Packed Beds of Solids BT - VDI
768 Heat Atlas, in: Springer Berlin Heidelberg, Berlin, Heidelberg, 2010: pp. 743–744.
769 https://doi.org/10.1007/978-3-540-77877-6_42.

770 [75] V. Gnielinski, Berechnung des Wärme-und Stoffaustauschs in durchströmten ruhenden
771 Schüttungen, (1982).

772 [76] V. Gnielinski, Equations for the calculation of heat and mass transfer during flow through
773 stationary spherical packings at moderate and high peclet numbers, Int. Chem. Eng. 21
774 (1981).

775 [77] S. Ergun, Fluid flow through packed columns, Chem. Eng. Prog. 48 (1952) 89–94.

776 [78] H.S. Fogler, S.H. Fogler, Elements of chemical reaction engineering, Pearson Educacion, 1999.

777 [79] N. Mladenov, J. Koop, S. Tischer, O. Deutschmann, Modeling of transport and chemistry in

channel flows of automotive catalytic converters, Chem. Eng. Sci. 65 (2010) 812–826. https://doi.org/10.1016/j.ces.2009.09.034.

[80] K. Herrera Delgado, L. Maier, S. Tischer, A. Zellner, H. Stotz, O. Deutschmann, Surface reaction kinetics of steam- and CO2-reforming as well as oxidation of methane over nickel-based catalysts, Catalysts. 5 (2015) 871–904. https://doi.org/10.3390/catal5020871.

[81] D. Chan, S. Tischer, J. Heck, C. Diehm, O. Deutschmann, Correlation between catalytic activity and catalytic surface area of a Pt/Al2O3 DOC: An experimental and microkinetic modeling study, Appl. Catal. B Environ. 156–157 (2014) 153–165. https://doi.org/10.1016/j.apcatb.2014.03.009.

[82] S. Saeidi, S. Najari, G. Gróf, F. Gallucci, Effect of operating conditions and effectiveness factor on hydrogenation of CO2 to hydrocarbons, Int. J. Hydrogen Energy. 44 (2019) 28586–28602. https://doi.org/10.1016/j.ijhydene.2019.08.255.

[83] A.M. Lattanzi, M.B. Pecha, V.S. Bharadwaj, P.N. Ciesielski, Beyond the effectiveness factor: Multi-step reactions with intraparticle diffusion limitations, Chem. Eng. J. 380 (2020) 122507. https://doi.org/10.1016/j.cej.2019.122507.

[84] P. Deuflhard, E. Hairer, J. Zugck, One-step and extrapolation methods for differential-algebraic systems, Numer. Math. 51 (1987) 501–516. https://doi.org/10.1007/BF01400352.

[85] M.A. Serrer, K.F. Kalz, E. Saraçi, H. Lichtenberg, J.-D. Grunwaldt, Role of Iron on the Structure and Stability of Ni3.2Fe/Al2O3 during Dynamic CO2 Methanation for P2X Applications, ChemCatChem. 11 (2019) 5018–5021. https://doi.org/10.1002/cctc.201901425.

[86] G.D. Wehinger, M. Ambrosetti, R. Cheula, Z.-B. Ding, M. Isoz, B. Kreitz, K. Kuhlmann, M. Kutscherauer, K. Niyogi, J. Poissonnier, R. Réocreux, D. Rudolf, J. Wagner, R. Zimmermann, M. Bracconi, H. Freund, U. Krewer, M. Maestri, Quo vadis multiscale modeling in reaction engineering? – A perspective, Chem. Eng. Res. Des. 184 (2022) 39–58. https://doi.org/10.1016/j.cherd.2022.05.030.

[87] T.S. Galhardo, A.H. Braga, B.H. Arpini, J. Szanyi, R. V Gonçalves, B.F. Zornio, C.R. Miranda, L.M. Rossi, Optimizing active sites for high CO selectivity during CO2 hydrogenation over supported nickel catalysts, J. Am. Chem. Soc. 143 (2021) 4268–4280. https://doi.org/10.1021/jacs.0c12689.

[88] J.Y. Lim, J. McGregor, A.J. Sederman, J.S. Dennis, Kinetic studies of CO2 methanation over a Ni/γ-Al2O3 catalyst using a batch reactor, Chem. Eng. Sci. 141 (2016) 28–45.

https://doi.org/10.1016/j.ces.2015.10.026.

[89] B. Kreitz, G.D. Wehinger, C.F. Goldsmith, T. Turek, Microkinetic Modeling of the CO2 Desorption from Supported Multifaceted Ni Catalysts, J. Phys. Chem. C. 125 (2021) 2984–3000. https://doi.org/10.1021/acs.jpcc.0c09985.

[90] S. Weber, R.T. Zimmermann, J. Bremer, K.L. Abel, D. Poppitz, N. Prinz, J. Ilsemann, S. Wendholt, Q. Yang, R. Pashminehazar, Digitization in Catalysis Research: Towards a Holistic Description of a Ni/Al2O3 Reference Catalyst for CO2 Methanation, ChemCatChem. 14 (2022) e202101878. https://doi.org/10.1002/cctc.202101878.

[91] J.C. Campuzano, R.G. Greenler, The adsorption sites of CO on Ni (111) as determined by infrared reflection-absorption spectroscopy, Surf. Sci. 83 (1979) 301–312. https://doi.org/10.1016/0039-6028(79)90495-3.

[92] A. Westermann, B. Azambre, M.C. Bacariza, I. Graça, M.F. Ribeiro, J.M. Lopes, C. Henriques, The promoting effect of Ce in the CO2 methanation performances on NiUSY zeolite: A FTIR In Situ/Operando study, Catal. Today. 283 (2017) 74–81. https://doi.org/10.1016/j.cattod.2016.02.031.

[93] T. Inul, M. Funabiki, Y. Takegami, Simultaneous methanation of CO and CO2 on supported Ni-based composite catalysts, Ind. Eng. Chem. Prod. Res. Dev. 19 (1980) 385–388. https://doi.org/10.1021/i360075a018.

[94] C. Heine, B.A.J. Lechner, H. Bluhm, M. Salmeron, Recycling of CO2: probing the chemical state of the Ni (111) surface during the methanation reaction with ambient-pressure X-ray photoelectron spectroscopy, J. Am. Chem. Soc. 138 (2016) 13246–13252. https://doi.org/10.1021/jacs.6b06939.

[95] B. Kreitz, P. Lott, J. Bae, K. Blöndal, S. Angeli, Z.W. Ulissi, F. Studt, C.F. Goldsmith, O. Deutschmann, Detailed Microkinetics for the Oxidation of Exhaust Gas Emissions through Automated Mechanism Generation, ACS Catal. 12 (2022) 11137–11151. https://doi.org/10.1021/acscatal.2c03378.

[96] H. Stotz, L. Maier, A. Boubnov, A.T. Gremminger, J.D. Grunwaldt, O. Deutschmann, Surface reaction kinetics of methane oxidation over PdO, J. Catal. 370 (2019) 152–175. https://doi.org/10.1016/j.jcat.2018.12.007.